Generation of nano-to-microplastics from polypropylene surfaces via femtosecond laser ablation in liquids with different viscosities

Haoyu Dong, Xi Huang, Zhipeng Wu, Peizi Li, Jean-François Silvain, Kazi Albab Hussain, Bai Cui, Yusong Li, Yongfeng Lu

Generation of Nano-to-microplastics from Polypropylene Surfaces via Femtosecond Laser Ablation in Liquids with Different Viscosities

Haoyu Dong[1], Xi Huang[1], Zhipeng Wu[1], Peizi Li[1], Jean-François Silvain[1, 3], Kazi Albab Hussain[2], Bai Cui[4], Yusong Li[2], Yongfeng Lu[1, *]

[1]Department of Electrical and Computer Engineering, University of Nebraska Lincoln, Nebraska, USA.

[2]Department of Civil and Environmental Engineering, University of Nebraska-Lincoln, Nebraska, USA.

[3]CNRS, University of Bordeaux; Bordeaux I.N.P., ICMCB, UMR 5026, F-33608 Pessac, France.

[4]Department of Mechanical and Materials Engineering, University of Nebraska Lincoln, Nebraska, USA.

**Corresponding authors:*

Yongfeng Lu, E-mail address: ylu2@unl.edu

Abstract

Preparation of polypropylene (PP) nano and microparticles, crucial for investigating the effects of plastics on both human health and the environment, presents a significant and immediate challenge. Utilizing an fs laser system in different liquid mediums such as water, dodecane, and hexadecane, we have successfully generated PP particles with sizes ranging from 1.8 to 4911 nm. This outcome is partly attributed to the constraint on plasma expansion caused by the viscosity of the liquid media. We investigated the areas of material removal and observed a transition from ordered to disordered removal patterns during this process. The formation of filaments and pillars within the material removal cavity, along with the deposition layer at the cavity edge, primarily occurred due to insufficient plasma formation at low laser energy levels. Furthermore, we observed neck-shaped filaments and nano cracks on the deposition surface, which were attributed to the heat effect during laser interaction with the PP substrate. Moreover, we collected distinct nano-Fourier transform infrared spectroscopy (FTIR) signals from both the nanoparticle area and the deposition

layer, revealing a 2 cm^{-1} wavenumber difference between the two regions. This discrepancy proved to be a valuable method for distinguishing between the nanoparticle area and the deposition layer.

Key words

Fs laser; polypropylene; nanoparticles; liquid media

1. Introduction

The inherent properties of various plastics, such as their corrosion resistance[1], ability to prevent biofouling[2], and stability maintenance[3], render them highly desirable for applications in industries like food packaging[4] and medical instruments[5]. However, during processes such as incineration [6], ablation[7, 8], and friction in plastic production, micro and nano plastic particles are generated. These tiny plastic particles are inadvertently ingested by humans through food[9], water[10, 11], and air [12, 13] consumption, yet they cannot be decomposed by cellular processes[14]. As a result, these particles accumulate in biological organs such as the pancreas[15], kidneys[16], and even embryos[17-19], posing potential health risks. Despite these concerns, the understanding of the metabolism and accumulation mechanisms of micro and nano plastic particles in organisms remains incomplete, leaving the extent of their threat to human health unclear. Meanwhile, microplastics pose a challenge in natural environments due to their resistance to degradation, contributing to air and water[20, 21] pollution. Thus, it is essential to acquire plastic particles of various sizes for a thorough analysis to determine their impact on organisms and the natural environment.

Lasers are a widely used tool for generating micro and nanoparticles due to their advantages, including versatility[22], high purity[23], and electro-affinity[24]. Pulsed laser ablation, whether in vacuum or liquid environments, stands out as one of the most widely employed techniques for

nanoparticle generation[25]. This method has been extensively utilized to produce nanoparticles of various materials such as Ni[26], ZnS[27], Si[28, 29], Ag[30, 31], and ZnO[32]. Researchers have employed different types of lasers, including ns[33], ps[34] and fs[35] lasers, with wavelengths spanning from UV to IR, to ablate the target surface and generate these nanoparticles. Metals and their oxide nanoparticles, generated through laser ablation, suggest the promising potential of utilizing lasers for nanoparticle production on polymer materials.

The field of laser micromachining and drilling has witnessed notable advancements in recent years, particularly in the processing of polymethyl methacrylate[36], polyimide[37], polyethylene[38], and polyetheretherkethone[39]. Researchers have explored the ablation and deposition of materials such as polytetrafluoroethylene[40] and polyetherimide[41], aiming to obtain thin film coatings on silicon substrates and microchannels. These studies have shed light on the interaction between lasers and polymer substrates, revealing that laser interaction results in the removal of a portion of the polymer material. However, despite these developments, there remains a critical gap in the literature regarding the potential use of lasers to generate polymer nanoparticles with controlled sizes. While numerous studies have explored the effects of lasers on polymers, none have specifically examined the potential of using lasers to generate with precise control of the sizes of polymer nanoparticles. Hence, the pressing task is to investigate the feasibility of laser-based methods for manufacturing polymer nanoparticles and to understand the fundamental mechanisms governing their formation.

This study explores the production of polypropylene (PP) nano and microparticles using fs laser ablation on a PP substrate in different liquids, such as water, dodecane, and hexadecane. A range of PP particles, spanning from 1.8 to 4911 nm, were produced using laser fluences of 3.86, 6.75 and 11.58 J/cm^2, with laser scanning speeds of 1 and 3 m/s. The research examines the effect of

bubble adhesion during laser ablation in water. Surface structures inside and outside the bubbles are compared to elucidate differences. Additionally, as the laser fluence increases from 3.86 to 11.58 J/cm^2, a transition from ordered to disordered material removal areas is observed in surface morphologies generated in dodecane and hexadecane. Insufficient plasma formation at 3.86 and 6.75 J/cm^2 is identified as the primary cause for the formation of filaments and pillars within the material removal cavity. Smooth deposition areas near the material removal cavity are also attributed to insufficient plasma formation. The interaction of the laser with the PP substrate also leads to heat effects, which are evident from the presence of neck-shaped filaments and nano-cracks on the deposition surface. To analyze the chemical compositions, different nano-FTIR signals are collected from both the nanoparticle area and the deposition layer, enabling the distinction between the two regions. A notable finding is the 2 cm^{-1} wavenumber difference observed between these two areas, which offers potential for distinguishing between the nanoparticle area and the deposition layer.

2. Experimental section

2.1 Materials

The commercial polypropylene (PP) food containers (2086752, Rubbermaid) were cut into 10 mm square sheets. Hexadecane (126805-500ML) and dodecane (215610-500ML), both 99% pure, were procured from Bean Town Chemical. Distilled water (15230147) from Thermo Fisher Scientific was used as the medium for laser ablation, while ethanol (EX0290-1) from Sigma-Aldrich was employed for ultrasonically cleaning the PP substrates. The PP substrates underwent separate ultrasonic cleaning cycles in ethanol and deionized water to ensure thorough cleaning and removal of residual organic contaminants. Subsequently, the cleaned PP substrates were dried overnight at 60°C before laser ablation.

2.2 Generation of polypropylene nanoparticles

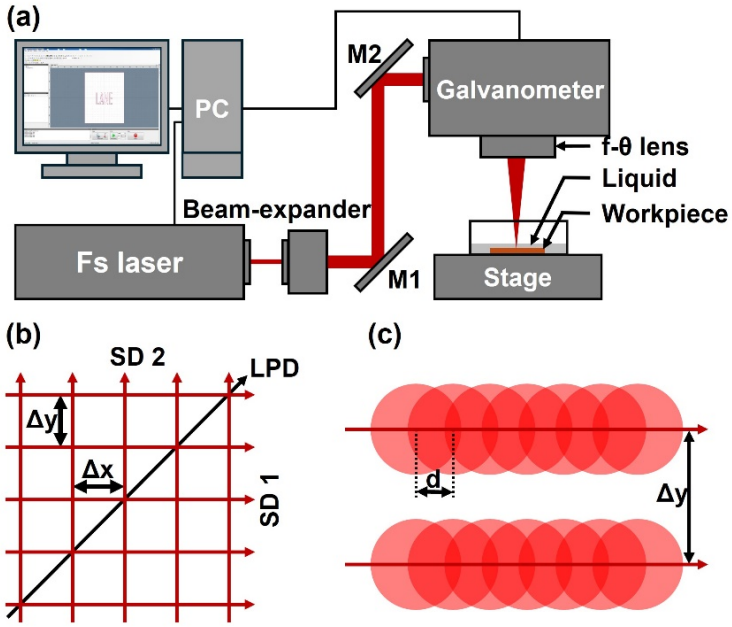

Fig. 1 Schematic of PP substrate fs laser processing. (a) The fs laser system setup, (b) two directions laser scanning strategy, and (c) pulse laser scanning overlap.

The PP particles were generated using a fs laser system (1030 nm wavelength, 405 fs pulse duration, Tangor, Amplitude Laser Inc.) employing a two-direction scanning strategy. The setup of the fs laser system is illustrated in Figure 1a. The output energy and frequency of the fs laser were monitored and controlled via PC software (Interface_v3.0.0). The pattern applied to the PP substrate was designed and managed by PC software (LaserDesk). The laser beam emitted by the fs laser source passed through a beam expander and total reflective mirrors before being directed into the galvanometer. (intelliSCAN III 14, SCANLAB GmbH). Following the galvanometer motion control, the laser beam was focused by an F-theta lens with a focal length of 70 mm. The PP substrate was positioned 2 mm below the surface of the respective liquid media, including water, dodecane, and hexadecane, with each liquid used separately.

A two- direction scanning strategy was employed to produce PP particles, as depicted in Figure 1b. The two scanning directions (SDs) are perpendicular and intersect with the laser polarization direction (PLD) at an angle of 45°. SD 1 is completed sequentially before SD 2 is initiated. The distances between adjacent scanning lines of SDs 2 and 1 were referred to as hatching distances Δx and Δy, respectively. To simplify the variables, Δx and Δy were both set to 30 μm in this study. The laser pulses, characterized by a Gaussian energy distribution, ablated the PP substrate through air and liquid media. The energy density at a specific position on the PP surface could be regulated by adjusting the distance (*d*) between two consecutive laser pulses, as illustrated in Figure 1c. The calculation of *d* was determined by the laser frequency and scanning speed, as per the following equation:

$$d = \frac{v}{f \times 10^3 - 1}, \tag{1}$$

where f is the laser frequency in kHz and ν is the scanning speed in m/s. In this study, a laser frequency of 330 kHz was utilized. Scanning speeds of 1 and 3 m/s were applied to the PP surfaces, corresponding to *d* values of 3.03 and 9.09 μm, respectively, to examine the influence of *d* on laser-induced particle sizes. Laser powers of 3, 7, and 13 W were applied to the PP surface at the same liquid layer thickness and laser scanning speed. The laser powers were measured using a power meter (Ophir Optronics Solutions, FL250A-BB-35). The pulse energies corresponding to 3, 7, and 13 W laser powers are 9.82, 17.18, and 29.45 μJ, respectively, as shown in Table 1. The focused beam diameter is 9 μm. The laser fluence (f) is influenced by the pulse energy and beam diameter following equation:

$$f = \frac{E}{A}, \tag{2}$$

where E is the laser pulse energy and A is the area of the laser spot. The fluence corresponds to 3, 7, and 13 W laser powers are 3.86, 6.75, and 11.58 J/cm², respectively. The processing times were fixed at 100 cycles using the same parameters, and the initial liquid temperature was maintained at 25°C. Following fs laser ablation, the PP substrate underwent a cleaning process involving a 10-minute ultrasonic treatment in ethanol, followed by drying in a 60°C oven. The liquid containing the generated nanoparticles was collected in brown glass bottles and then subjected to a 5-minute ultrasonic treatment to ensure even dispersion of the nanoparticles within the liquid.

Table. 1 Laser pulse energies and fluences with different laser powers

Power (W)	Pulse energy (μJ)	Fluence (J/cm^2)
3	9.82	3.86
7	17.18	6.75
13	29.45	11.58

2.3 Characterization

The surface structures of the PP substrates were obtained using a scanning electron microscope (FEI Helios NanoLab 660) following a 6 nm Au coating process conducted with a sputtering system (AJA International Orion Series Sputtering Systems). A particle size analyzer (Zeta Potential Analyzer) was employed to analyze the size distribution of PP particles in liquid. For particle size analysis, 2 mL of ultrasonically treated homogeneous liquid was used. The surface chemical composition of the Au-coated PP substrates was analyzed using localized infrared (IR) spectroscopy with an Anasys nanoIR2-s system. Images captured after fs laser ablation were obtained using a Navitar lens equipped with uEye Cockpit software-controlled CCD camera.

3. Result and discussion

3.1 Particle size distributions

The numbers of particle sizes in different media at specific fluence and scanning speed were normalized during data collection by the Zeta Potential Analyzer and its software. The distributions obtained using the same laser fluence and scanning speed but in various liquids were gathered in a single image, as illustrated in Fig. 2. Distinct peaks representing the highest normalized particle numbers were observed for each medium across all fluence and scanning speed settings. In Fig. 2, the positioning of the six images was determined by coordinates (x, y) corresponding to scanning speed and fluence. The particle diameters observed across various experimental groups ranged from 1.8 to 4911 nm. Notably, as scanning speed increased from 1 to 3 m/s, the particle diameters decreased to varying degrees when using the same fluence and medium. With increasing laser fluence, the particle diameters in water increased from 130.8 to 256.4 nm at 1 m/s scanning speed, and from 1.8 to 702.2 nm at 3 m/s scanning speed. Conversely, in dodecane, the particle diameters remained relatively constant, approximately 2400 nm at 1 m/s scanning speed and about 1900 nm at 3 m/s scanning speed. However, in hexadecane, the diameters increased from 5.5 to 2819.1 nm at 3 m/s scanning speed as laser fluence increased. Interestingly, at 1 m/s scanning speed, the particle diameter processed in hexadecane initially decreased from 3360.3 to 1013.3 nm and then increased to 4911.5 nm as laser fluence increased. Analysis of specific coordinate pairs (3, 3.86), (1, 6.75), and (3, 6.75) revealed a consistent trend where particle diameter processed in water was the smallest, while in dodecane, it was the largest among the three media. Conversely, coordinate pairs (1, 3.86), (1, 11.58), and (3, 11.58) exhibited a consistent trend where the largest particle diameter was processed in hexadecane, while the smallest was processed in water. Furthermore, coordinate pairs (1, 11.58) and (3, 11.58) demonstrated two distinct particle size distribution intervals in water, ranging from 113 to 140.4 nm and 215.6 to 304.9 nm for (1, 11.58), and 145.9 to 194.1 nm and 653.8 to 702.2 nm for (3, 11.58), respectively.

The observation of two or three main peaks in the particle diameter distribution plots, as depicted in Fig. S1, when the normalized density was applied as the y-axis, indicates that the laser interaction with the PP substrate resulted in the production of particles across two different diameter scales. The presence of multiple peaks in the normalized density plot suggests variations in particle size distribution. In these plots, a strong peak is generated for larger particle diameters due to their larger volumes, even if they are represented by fewer particles. Conversely, weaker normalized density is observed for smaller diameter particles since their total volume is smaller compared to larger diameter particles. Consequently, the ratio of the number of larger to smaller particles tends towards zero, resulting in fewer peaks being observed in the normalized particle number plots.

The masses of PP in media at different laser fluences and scanning speeds are depicted in Fig. S2. The masses of PP in media were calculated by weighing 500 µL of liquids after fs laser processing and ultrasound treatment. The densities of PP, water, hexadecane, and dodecane are 0.9, 0.9981, 0.7602, and 0.7430 g/mL at 20°C and local pressure. The calculated masses of PP range from 0.00342 to 0.06048 g/mL. As laser fluence increases, the mass of PP also increases. However, as scanning speed increases, the mass of PP does not show an obvious trend. This is because some of the produced PP escaped from the liquid along with the movement of bubbles formed by laser-material interactions. The highest mass of PP in media for laser fluences of 3.86, 6.75, and 11.58 J/cm² was observed at scanning speeds of 3 m/s in dodecane, 1 m/s in water, and 3 m/s in hexadecane, respectively.

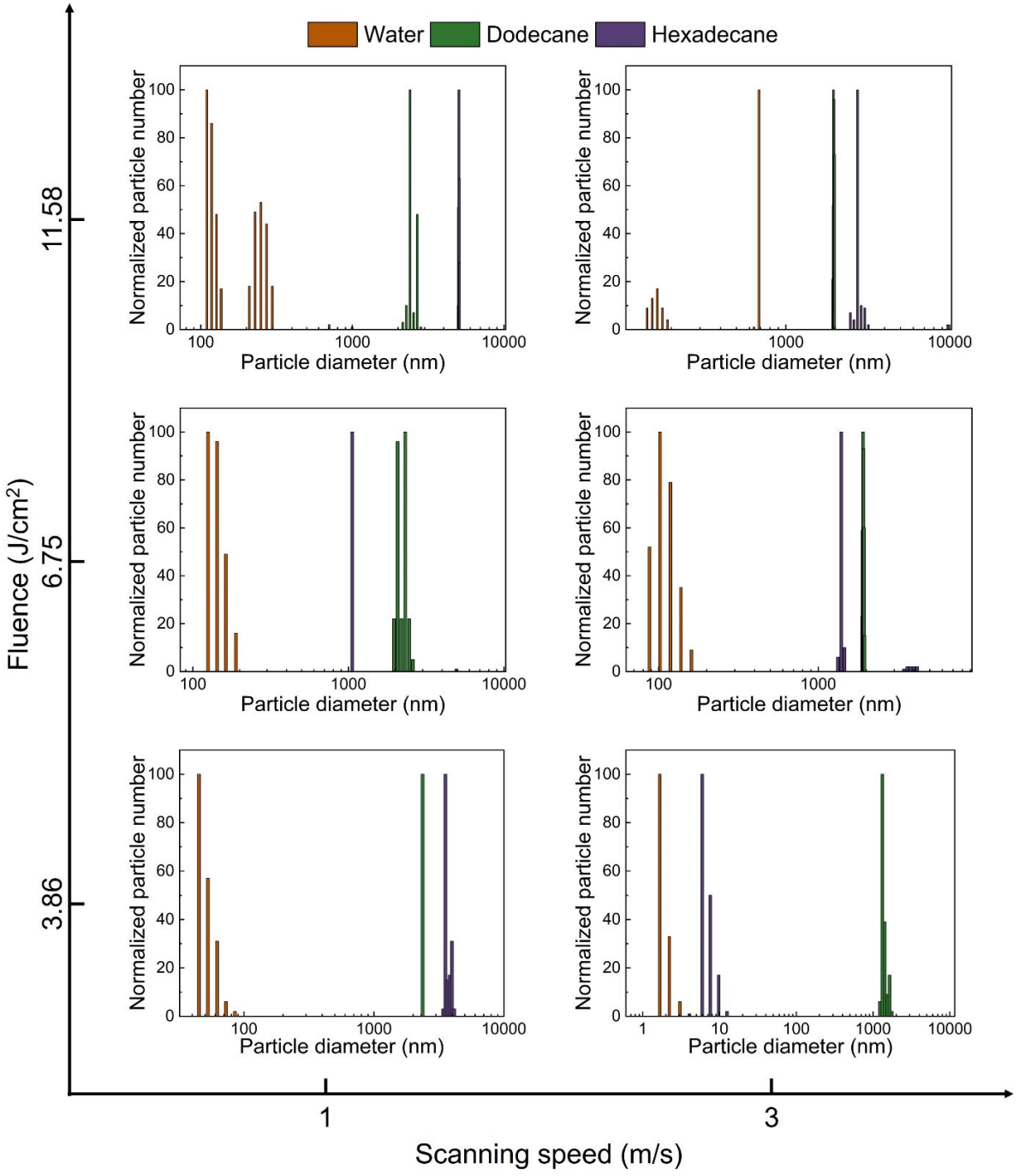

Fig. 2 Particle diameter distributions in water, dodecane, and hexadecane with fluence and scanning speed changing.

The particle diameter varied by over 1000 nm under the same laser fluence and scanning speed across different liquid types, as illustrated in Fig. 2. The variability of different media is attributed to the main influencing factor affecting particle diameter. During laser-substrate interaction, plasma is generated, the expansion of which is impeded by the liquid medium to varying extents owing to differences in viscosity. The viscosities of water, dodecane, and hexadecane utilized in the experiment are 0.89, 1.34, and 3.06 mPa·s, respectively. As viscosity increases, plasma cooling occurs within a smaller spatial range, resulting in the formation of larger particles. Additionally, changes in particle diameters were observed with variations in laser fluence and scanning speed. This phenomenon is attributed to the laser density, primarily determined by laser fluence, which influences the generation of plasma to different levels, thus leading to variations in particle diameter. In summary, the two main factors affecting particle diameter are the sufficient level of plasma generated by laser fluence and the degree to which the viscosity of the liquid medium inhibits plasma diffusion.

3.2 Bubble adhesion behaviors

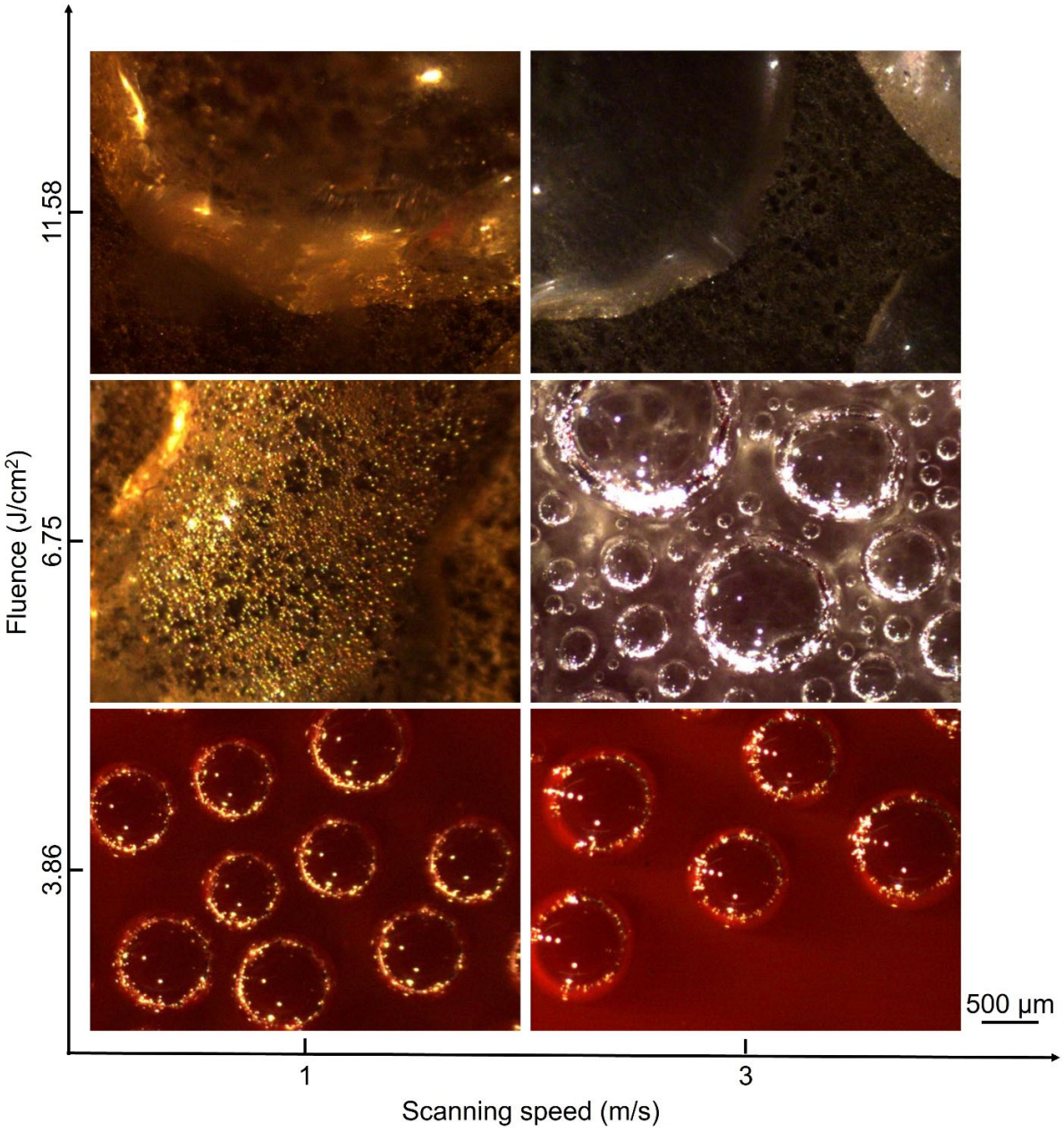

Fig. 3 Bubble adhesion behaviors after fs laser ablation in water

During fs laser ablation, the presence of bubbles was observed, particularly evident when processing in water, as depicted in Fig. 3. The distribution and size conditions of these bubbles are illustrated in Fig. 3, while Figs. S3 and S4 show the absence of bubble adhesion behaviors after fs laser ablation in dodecane and hexadecane, respectively. In water, the bubbles are filled with H_2

and O_2 [42, 43], whereas in dodecane and hexadecane, the bubbles are filled with H_2 and hydrocarbons [44, 45]. In water, notable bubble adhesion behaviors were observed, with the number and size of bubbles varying depending on the processing conditions. For instance, when applying 3.86 J/cm^2 fluence to the PP substrate, bubbles were observed even on the substrate surface. When the scanning speed was set to 1 m/s, 5 full bubbles were observed on the treated PP substrate surface, whereas 9 full bubbles were observed at 3 m/s processing speed. This difference in bubble formation can be attributed to the total laser energy per unit area, which triples when decreasing the scanning speed from 3 to 1 m/s, leading to more bubbles formed on the substrate surfaces. Moreover, as the laser fluence increased from 3.86 to 6.75 J/cm^2, the PP substrate surface treated at 3 m/s scanning speed exhibited a disordered distribution of bubbles, with variations in both size and location. Notably, the diameter of the largest bubble continuously increased with increasing laser fluence. Additionally, two bubbles were observed to merge upon contact, causing them to extrude and lose their spherical shape, as depicted in Fig. 3 for coordinates (1, 7), (1, 13), and (3, 13). Concurrently, the color of the PP substrate surface darkened from red to black as the laser fluence increased. In contrast, when laser ablation was performed in dodecane and hexadecane, the formed bubbles did not adhere to the substrate surface. Consequently, no adhesive bubbles were observed on the PP substrate surface after laser ablation, as shown in Figs. S3 and S4.

3.3 Surface morphologies

The surface morphologies resulting from fs laser ablation in water and the underlying mechanisms shaping the structure formed on the PP substrate are elucidated in Fig. 4. Upon laser ablation in water, two distinct features were observed on the PP substrate surface. Firstly, circularly shaped laser interaction areas were evident outside the bubble, while relatively smooth areas were

observed inside the bubble, as depicted in Fig. 4c. Notably, Fig. 4d illustrates the presence of an obvious material removal feature. The measured diameter of the circle was found to be 47 μm, significantly larger than the effective laser beam focus diameter of 9 μm. The size difference between the formed circle shown in Fig. 4d and the diameter of the laser beam suggests that the circular area resulted from the accumulation of multiple laser pulses at this specific location. This accumulation includes the influence of adjacent pulses affected by the liquid medium and repeated cycles using the same parameters. The ablation of the PP substrate by the laser beam evaporated and ionized the material [46] and led to the formation of plasma, as depicted in Fig. 4a. However, the expansion of the plasma was impeded by the viscosity and mass of the water medium. Concurrently, during the formation of plasma, the PP substrate underwent tearing, with a portion of it being deposited on the edges, subsequently forming a deposition layer, as illustrated in Fig. 4d.

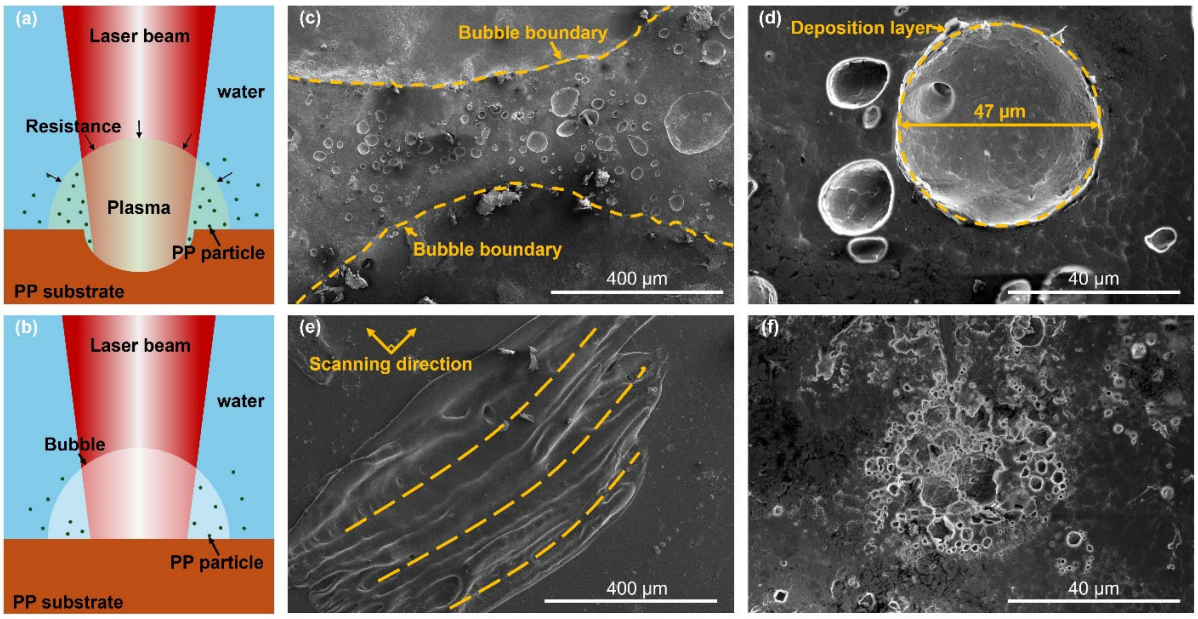

Fig. 4 Surface morphologies after laser ablation in water and the mechanisms. (a-b) mechanism of structure formed by fs laser and PP substrate interaction without bubble and with bubble,

respectively. (c) Bubble boundary. (d-f) Laser processed surface outside the bubble, at the center of the bubble, and at the edge of the bubble.

At the water-bubble interface, the laser beam exhibited reflection and refraction, as illustrated in Fig. 4b. Upon passing through the center of the bubble, the laser beam was refocused and interacted with the PP substrate. As a result, a similar ablation pattern to that observed in air was obtained at the center area of the bubble on the PP surface, as depicted in Fig. 4e. However, the melting path, indicated by yellow dashed lines in Fig. 4e, appeared as a series of curves. This curvature stemmed from the shifting of laser focus positions, attributed to the fact that the top of the bubble was not completely flat. Additionally, small and disordered areas of PP removal were identified near the boundary of the bubble within the bubble itself, as shown in Fig. 4f. The laser focus position remained relatively stable in this region due to its proximity to the bubble interface. As a result, the laser energy decreased, leading to reduced processing capability in this area and causing the formation of small, disordered material removal.

Unlike archetypal multi-filaments phenomenon, which is periodic and well controlled, in metals [47], ceramics [48], and polymers [49], the surface morphologies following laser ablation in hexadecane are depicted in Fig. 5. In Fig. 5a, it is evident that the laser pulses accumulated at the crossing points of the scanning paths, resulting in an area where the total laser power input doubled compared to other scanning paths. Consequently, material removal areas expanded at these crossing points, coinciding with the two SDs, as illustrated in Fig. 5b. However, as the laser fluence increased from 6.75 to 1.58 J/cm^2, the extension trends of the material removal areas became less defined, eventually becoming indistinct, as shown in Figs. 5c and 5d. This is attributed to the enlargement of bubbles and the increased influence area of previous interactions between the laser

and the PP substrate. Consequently, the laser beam underwent reflection, scattering, and refocusing before reaching the PP substrate, resulting in misty and disordered processing results.

A similar transition from order to disorder was observed in both dodecane and hexadecane as the laser fluence increased, while maintaining the same scanning speed, as depicted in Figs. S5 and S6. Remarkably, continuous material removal areas were observed along SD 2 when applying 3.86 J/cm^2 laser fluence and 1 m/s scanning speed in hexadecane, as illustrated in Fig. S6. Likewise, in dodecane, the transition of material removal areas from discrete to continuous was observed when applying 3.86 J/cm^2 laser fluence and 1 m/s scanning speed., as depicted in Fig. S7. This phenomenon suggests that a more orderly processed substrate can be achieved by reducing the processing fluence and increasing the number of processing times. However, it is important to note that this approach sacrifices processing efficiency.

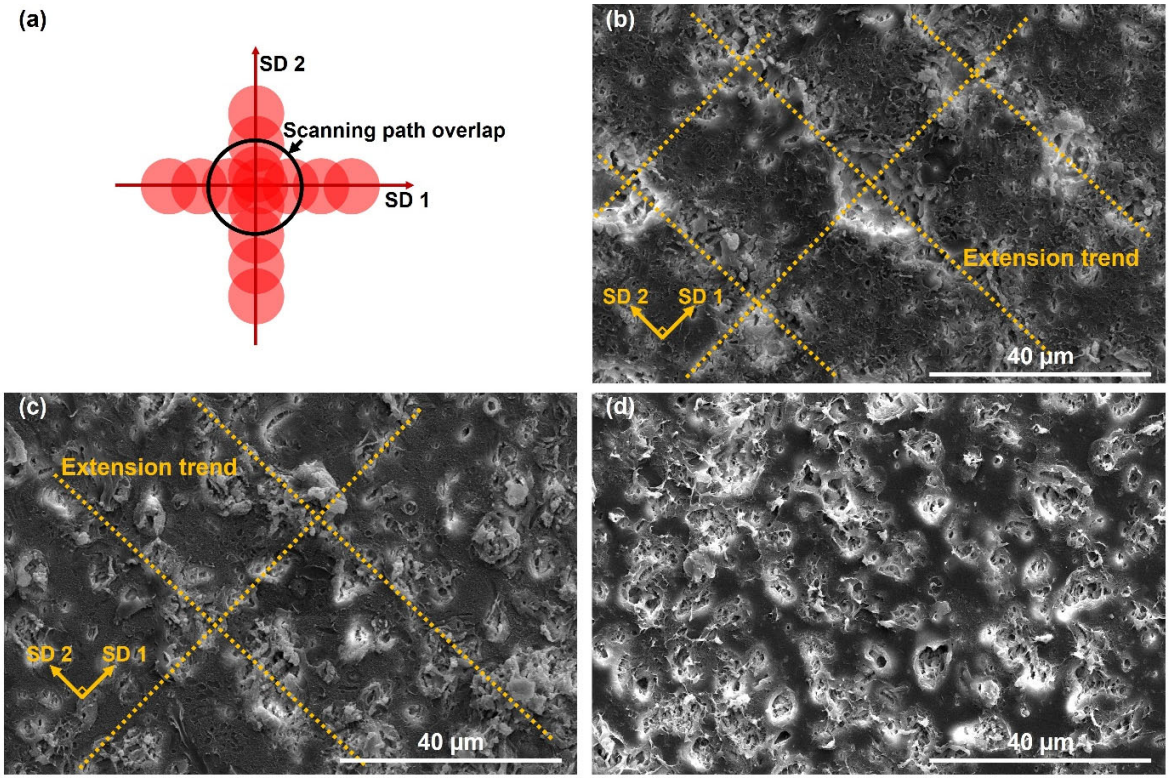

Fig. 5 Surface morphologies after laser processing in hexadecane and material remove area distribution. (a) Two scanning paths overlap during laser ablation. (b-d) 3.86, 6.75, and 11.58 J/cm^2 fluence with 3 m/s scanning speed fs laser ablated PP substrate surface in hexadecane, respectively.

The surface morphologies within the material removal areas in dodecane and hexadecane are illustrated in Fig. 6. When laser ablated the PP substrate in dodecane, as shown in Fig. 6a, filaments were observed within the material removal area. This formation can be attributed to insufficient plasma formation and subsequent cooling and re-solidification of plasma within the cavity. The interweaving of filaments inside the material removal cavity suggests a complex interaction between the laser pulses and the material. As the filament area enlarged, neck-shaped elongated filaments and nano cracks were observed as illustrated in Fig. 6b, indicating the presence of thermal effects during the laser-material interaction. Notably, the direction of the nano cracks is perpendicular to the direction of the filament, suggesting a tensile stress distribution within the filament.

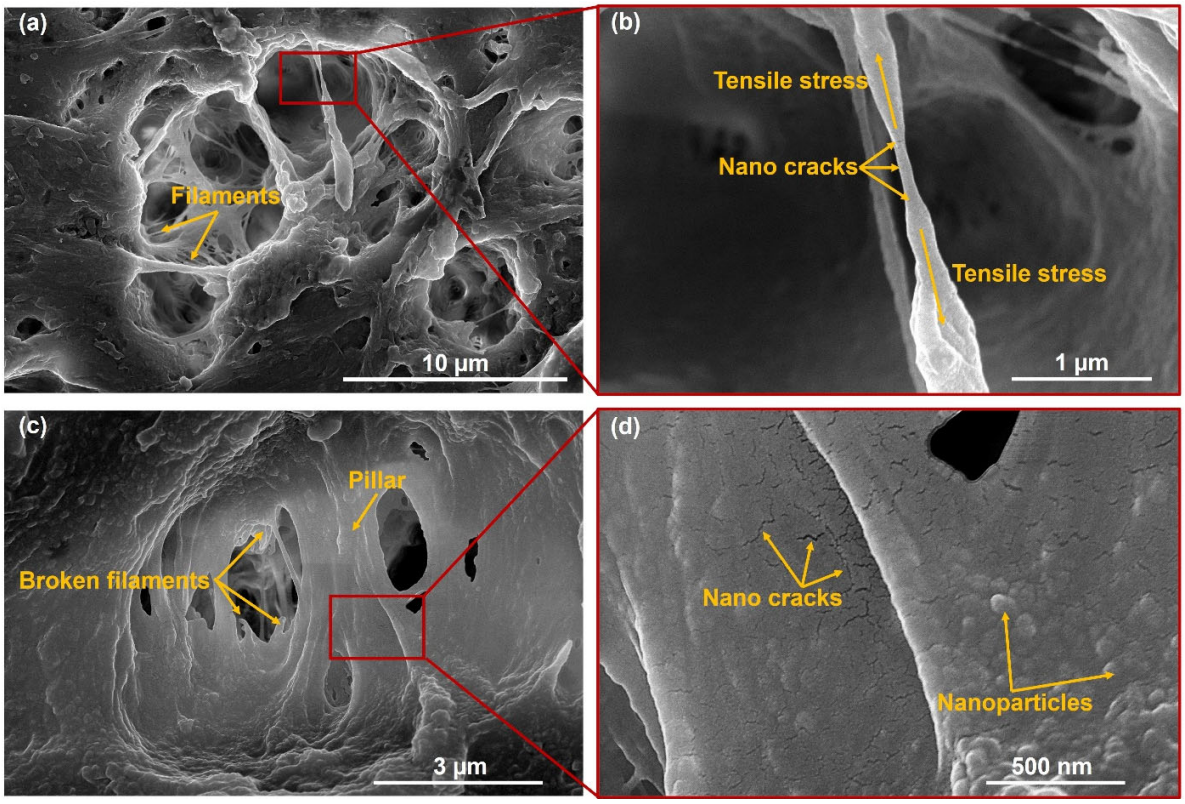

Fig. 6 Surface morphologies inside the material removal areas. (a) Material removal area in dodecane. (b) Tensile stress on the filament. (c) Material removal area in hexadecane. (d) Nano cracks and nanoparticles on the pillar.

In contrast, when hexadecane was employed as the medium liquid, a portion of the filaments evolved into pillars within the material removal area as shown in Fig. 6c. This transformation suggests encountering greater resistance during the plasma escape process, leading to the formation of the pillars. Additionally, broken filaments were observed within the material removal cavity. Furthermore, nano cracks and nanoparticles were found at the root of the pillars (Fig. 6d). The orientation of the nano cracks, perpendicular to the extension direction of the pillar, indicates the presence of tensile stress along the pillars. Additionally, the presence of nanoparticles attached to the pillars and inner cavity indicates that some nanoparticles were unable to escape from the material removal cavity, resulting in their deposition onto nearby surfaces.

The surface morphologies near the material removal areas at high magnification are illustrated in Fig. 7. In Fig. 7a, nanoparticles and deposition layers are observed near the material removal cavity. Insufficient plasma formation, particularly evident at a low laser fluence of 3.86 J/cm^2, caused some materials to remain in the solid phase and escape from the cavity. The deposition layer formed as solid material attached to the cavity edge. This phenomenon is confined to the vicinity of the cavity due to the hindrance of the liquid medium and the weight of the solid material, preventing the deposition layer from spreading further. Additionally, some nanoparticles were deposited on the material surface, forming a nanoparticle area, while others were dispersed into the liquid medium.

As the laser fluence increased from 3.86 to 6.75 J/cm^2, the effects of insufficient plasma formation were mitigated, resulting in a reduced number and size of the deposition areas as marked in Fig. 7b. Eventually, at a laser fluence of 11.58 J/cm^2 (Fig. 7c), the deposition layer disappeared entirely because the plasma group generated was sufficient and did not contain solid-phase material. A similar deposition layer was observed when laser ablation was performed using low laser fluences in hexadecane as shown in Fig. S8a. Additionally, disordered nano cracks were found on the surface of the deposition layer under high magnification, indicating the presence of tensile stress and heat effects on the deposition layer as illustrated in Fig. S8b.

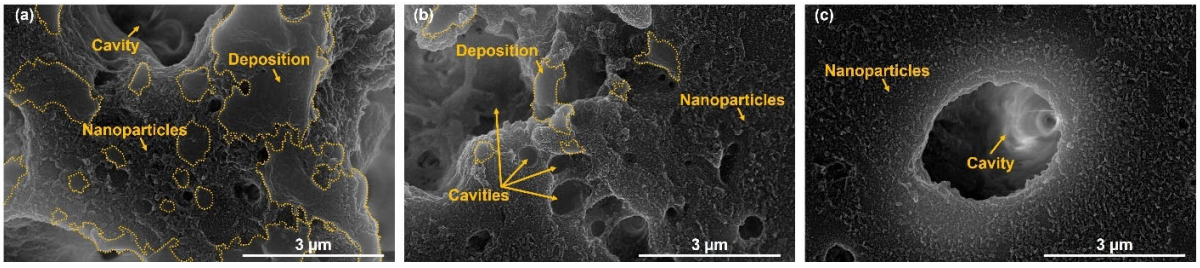

Fig. 7 Surface morphologies near the material removal areas. (a-c) 3.86, 6.75, and 11.58 J/cm^2 fluence with 3 m/s scanning speed fs laser ablated PP substrate surface in dodecane, respectively.

3.4 Chemical compositions

The chemical compositions and surface morphologies were acquired within a 2.5 μm square area using a nano-FTIR system, as illustrated in Fig. 8. The boundary between the nanoparticles and deposition was clearly distinguished in the deflection mapping shown in Fig. 8a. The topography of the scanned 2.5 μm square is depicted in Fig. S9. A height profile along the white line marked in Fig. 8a is shown in Fig. 8c. It reveals that altitude changes in the nanoparticle area were within 150 nm with fluctuations, whereas altitude changes in the deposition area exceeded 350 nm and appeared smooth.

While nano cracks similar to those depicted in Fig. S8 were not identifiable in the nano-FTIR system due to its relatively large tip resolution of 30 nm, the system effectively recorded the amplitude collected at 1376 cm^{-1} [50] using signals discerned by a threshold of 0.1 V and an optimized molecular resonance frequency ranging from 126 to 186 kHz, as illustrated in Fig. 8b. The wavenumbers were found to shift at different distances after undergoing various material plasmaization, heating, and cooling processes in both the nanoparticle area and deposition layer, as shown in Fig. 8d. The intensity of the nanoparticle area appeared slightly higher than that of the deposition layer, primarily caused by the limited enhancement of IR signals by gold particles on the substrate surface. The peak for the nanoparticle area was measured at 1370 cm^{-1}, while for the deposition area, it was at 1368 cm^{-1}. Compared with the original substrate surface peak at 1376 cm^{-1}, the peaks shift differently in nanoparticle and deposition areas. Despite the subtle differences between the two peaks, the nanoparticle area and deposition layer were successfully distinguished by the IR mapping. Notably, the maximum molecular resonance frequency for the nanoparticle and deposition areas were found to be 146 and 174 kHz, respectively, indicating that the nanoparticle area was softer than the deposition area.

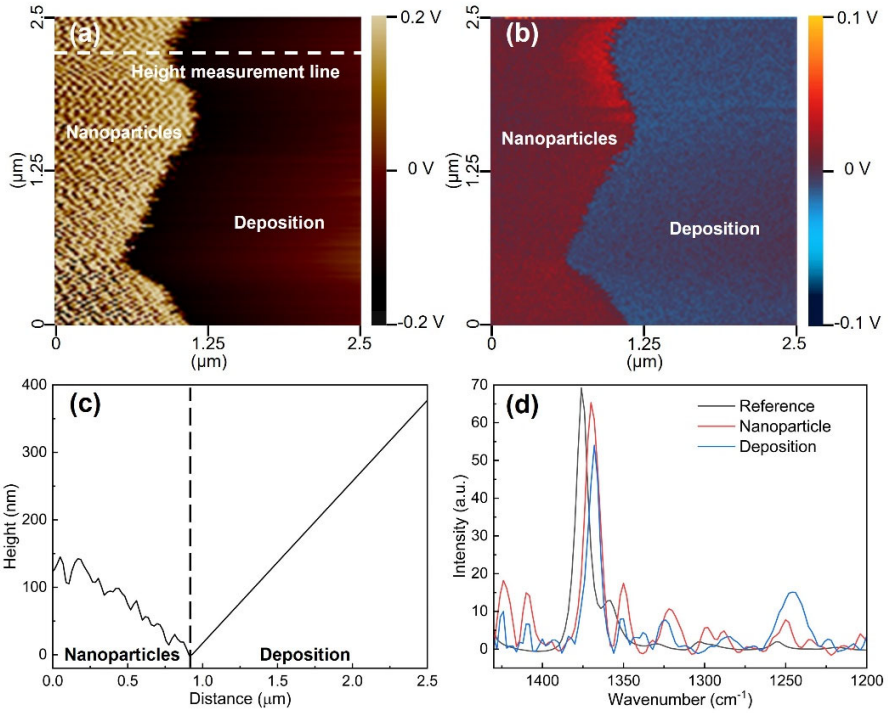

Fig. 8 Chemical compositions of the laser ablated surface. (a) Deflection mapping on ablated surface. (b) Amplitude mapping on ablated surface. (c) Height change along the line. (d) Local infrared spectrum of nanoparticle and deposition area.

4. Conclusions

In summary, this study successfully generated nano and microparticles with diameters ranging from 1.8 to 4911 nm on the surface of commercial PP containers for research purposes, utilizing an fs laser system in various liquid media. The differences in particle sizes are primarily driven by two factors: the sufficient level of plasma generated by the laser fluence and the degree to which the viscosity of the liquid medium inhibits plasma diffusion. The investigation explored the adverse effects of bubble adhesion behavior on the laser processing capability of the PP substrate surface, comparing outcomes obtained both outside and inside bubbles. Moreover, the study observed a transition from ordered to disordered surfaces as the laser fluence increased from 3.86

to 11.58 J/cm^2, highlighting the influence of bubble formation on processing outcomes at higher laser fluences. The formation of filaments and pillars within the material removal cavity is attributed to insufficient plasma formation during laser-material interactions. Furthermore, the study identified that insufficient plasma formation at laser fluences of 3.86 and 6.75 J/cm^2 led to the formation of smooth deposition layers outside the material removal cavity. The presence of neck-shaped elongated filaments and nano cracks on the deposition surface provided evidence of heat effects during fs laser interaction with the PP substrate. Additionally, nano-FTIR analysis revealed shifts in peak positions due to various formation reasons, including plasma-cooled nanoparticles and material torn apart from the substrate. These findings deepen our understanding of the mechanisms underlying fs laser ablation of PP substrates and offer valuable insights for future research in this domain. The methodology employed in this research can be readily adapted for the generation of plastic particles from other materials, such as polyethylene and polyethylene terephthalate.

CRediT authorship contribution statement

Haoyu Dong: Methodology, Data curation, Formal analysis, Investigation, Validation, Writing-original draft, Writing-review & editing. **Xi Huang:** Formal analysis**,** Validation. **Zhipeng Wu:** Methodology. **Peizi Li:** Methodology. **Bai Cui:** Resources, Funding acquisition. **Jean-François Silvain:** Resources, Funding acquisition. **Yusong Li:** Resources, Funding acquisition. **Kazi Albab Hussain:** Data curation. **Yongfeng Lu:** Resources, Conceptualization, Funding acquisition, Supervision, Project administration, Writing-review & editing.

Declaration of Competing Interest

The authors declare that they have no known competing financial interests or personal relationships that could have appeared to influence the work reported in this paper.

Data availability

Data will be made available on request.

Acknowledgment

This work is partially supported by the University of Nebraska-Lincoln Grand Challenge Catalyst Project titled 'Release of Micro- and Nanoplastics from Plastic Food Containers: Characterization, Risk Assessment, Socioeconomic, and Health Impacts". This work was partly performed at the Nano-Engineering Research Core Facility (NERCF), which is partially funded by the Nebraska Research Initiative.

Appendix A. Supplementary material

Supplementary data to this article can be found in the attached files.

References

[1] Y.S. Xie, J.R. Jiang, M.A. Islam, Elastomers and plastics for resisting erosion attack of abrasive/erosive slurries, Wear, 426 (2019) 612-619.

[2] V. Freitas, O. Gonçalves, M. Dolbeth, S. Ramos, J. Morais, R.O.D. Ozorio, I. Martins, J.R. Almeida, Optimization of plastic polymers for shellfish aquaculture infrastructures: in situ antifouling performance assessment, Frontiers in Marine Science, 10 (2023).

[3] A. Gushchin, E. Mallada, A. Tang, Phase-Coupled Oscillators with Plastic Coupling: Synchronization and Stability, Ieee Transactions on Network Science and Engineering, 3 (2016) 240-256.

[4] H. Liu, W.C. Xu, D.L. Li, Development of New Plastic Packaging Film for Food Packaging, in: 49th Conference of the International-Circle-of-Educational-Institutes-for-Graphic-Arts-Technolo gy-and-Management / 8th China Academic Conference on Printing and Packaging, China Acad Printing Technol, Beijing, PEOPLES R CHINA, 2017, pp. 805-810.

[5] M.W. Dou, S.T. Sanjay, D.C. Dominguez, P. Liu, F. Xu, X.J. Li, Multiplexed instrument-free meningitis diagnosis on a polymer/paper hybrid microfluidic biochip, Biosensors & Bioelectronics, 87 (2017) 865-873.

[6] A. Borysov, A. Tarasenko, N. Krisanova, N. Pozdnyakova, A. Pastukhov, M. Dudarenko, K. Paliienko, T. Borisova, Plastic smoke aerosol: Nano-sized particle distribution, absorption/fluorescent properties, dysregulation of oxidative processes and synaptic transmission in rat brain nerve terminals, Environmental Pollution, 263 (2020) 114502.

[7] D. Magrì, P. Sánchez-Moreno, G. Caputo, F. Gatto, M. Veronesi, G. Bardi, T. Catelani, D. Guarnieri, A. Athanassiou, P.P. Pompa, D. Fragouli, Laser Ablation as a Versatile Tool To Mimic Polyethylene Terephthalate Nanoplastic Pollutants: Characterization and Toxicology Assessment, ACS Nano, 12 (2018) 7690-7700.

[8] I. Kanehara, H. Yamashita, S. Fujii, T. Kimura, M. Yamamoto, T. Tanabe, Nano-Sized Polyethylene Particles Produced by Nano-Second UV Laser Ablation, Lasers in Manufacturing and Materials Processing, 10 (2023) 389-399.

[9] B. Toussaint, B. Raffael, A. Angers-Loustau, D. Gilliland, V. Kestens, M. Petrillo, I.M. Rio-Echevarria, G. Van den Eede, Review of micro- and nanoplastic contamination in the food chain, Food Additives and Contaminants Part a-Chemistry Analysis Control Exposure & Risk Assessment, 36 (2019) 639-673.

[10] Y.H. Huang, K.K. Wong, W. Li, H.R. Zhao, T.M. Wang, S. Stanescu, S. Boult, B. van Dongen, P. Mativenga, L. Li, Characteristics of nano-plastics in bottled drinking water, Journal of Hazardous Materials, 424 (2022).

[11] A. Winkler, F. Fumagalli, C. Cella, D. Gilliland, P. Tremolada, A. Valsesia, Detection and formation mechanisms of secondary nanoplastic released from drinking water bottles, Water Research, 222 (2022).

[12] E. Caracci, A. Vega-Herrera, J. Dachs, N. Berrojalbiz, G. Buonanno, E. Abad, M. Llorca, T. Moreno, M. Farré, Micro(nano)plastics in the atmosphere of the Atlantic Ocean, Journal of Hazardous Materials, 450 (2023).

[13] D.H. Luo, X.Y. Chu, Y. Wu, Z.F. Wang, Z.L. Liao, X.L. Ji, J.J. Ju, B. Yang, Z. Chen, R. Dahlgren, M.H. Zhang, X. Shang, Micro- and nano-plastics in the atmosphere: A review of occurrence, properties and human health risks, Journal of Hazardous Materials, 465 (2024).

[14] T.R. Gaspar, R.J. Chi, M.W. Parrow, A.H. Ringwood, Cellular Bioreactivity of Micro- and Nano-Plastic Particles in Oysters, Frontiers in Marine Science, 5 (2018).

[15] S. Haldar, Y. Muralidaran, D. Míguez, S.I. Mulla, P. Mishra, Eco-toxicity of nano-plastics and its implication on human metabolism: Current and future perspective, Science of The Total Environment, 861 (2023) 160571.

[16] X. Meng, J. Zhang, W. Wang, G. Gonzalez-Gil, J.S. Vrouwenvelder, Z. Li, Effects of nano- and microplastics on kidney: Physicochemical properties, bioaccumulation, oxidative stress and immunoreaction, Chemosphere, 288 (2022) 132631.

[17] T.Ö. Sökmen, E. Sulukan, M. Türkoğlu, A. Baran, M. Özkaraca, S.B. Ceyhun, Polystyrene nanoplastics (20 nm) are able to bioaccumulate and cause oxidative DNA damages in the brain tissue of zebrafish embryo (Danio rerio), NeuroToxicology, 77 (2020) 51-59.

[18] Z. Duan, X. Duan, S. Zhao, X. Wang, J. Wang, Y. Liu, Y. Peng, Z. Gong, L. Wang, Barrier function of zebrafish embryonic chorions against microplastics and nanoplastics and its impact on embryo development, Journal of Hazardous Materials, 395 (2020) 122621.

[19] C. Della Torre, E. Bergami, A. Salvati, C. Faleri, P. Cirino, K.A. Dawson, I. Corsi, Accumulation and Embryotoxicity of Polystyrene Nanoparticles at Early Stage of Development of Sea Urchin Embryos Paracentrotus lividus, Environmental Science & Technology, 48 (2014) 12302-12311.

[20] M. Shams, I. Alam, I. Chowdhury, Aggregation and stability of nanoscale plastics in aquatic environment, Water Research, 171 (2020).

[21] N. Navarre, J.M. Mogollón, A. Tukker, V. Barbarossa, Recycled plastic packaging from the Dutch food sector pollutes Asian oceans, Resources Conservation and Recycling, 185 (2022).

[22] S. Barcikowski, G. Compagnini, Advanced nanoparticle generation and excitation by lasers in liquids, Phys Chem Chem Phys, 15 (2013) 3022-3026.

[23] W.-j. Jeong, J. Bu, L.J. Kubiatowicz, S.S. Chen, Y. Kim, S. Hong, Peptide–nanoparticle conjugates: a next generation of diagnostic and therapeutic platforms?, Nano Convergence, 5 (2018) 38.

[24] H. Muto, K. Yamada, K. Miyajima, F. Mafuné, Estimation of Surface Oxide on Surfactant-Free Gold Nanoparticles Laser-Ablated in Water, The Journal of Physical Chemistry C, 111 (2007) 17221-17226.

[25] A.M. El-Khawaga, A. Zidan, A.I.A.A. El-Mageed, Preparation methods of different nanomaterials for various potential applications: A review, Journal of Molecular Structure, 1281 (2023) 135148.

[26] B. Liu, Z.D. Hu, Y. Che, Y.B. Chen, X.Q. Pan, Nanoparticle generation in ultrafast pulsed laser ablation of nickel, Applied Physics Letters, 90 (2007).

[27] M. Oujja, I. Lopez-Quintas, A. Benítez-Cañete, R. de Nalda, M. Castillejo, Harmonic generation by atomic and nanoparticle precursors in a ZnS laser ablation plasma, Applied Surface Science, 392 (2017) 572-580.

[28] K. Momoki, T. Manabe, L. Li, J.W. Yan, Silicon nanoparticle generation and deposition on glass from waste silicon powder by nanosecond pulsed laser irradiation, Materials Science in Semiconductor Processing, 111 (2020).

[29] S.I. Kudryashov, A.A. Nastulyavichus, A.K. Ivanova, N.A. Smirnov, R.A. Khmelnitskiy, A.A. Rudenko, I.N. Saraeva, E.R. Tolordava, A.Y. Kharin, I.N. Zavestovskaya, Y.M. Romanova, D.A. Zayarny, A.A. Ionin, High-throughput laser generation of Si-nanoparticle based surface coatings for antibacterial applications, Applied Surface Science, 470 (2019) 825-831.

[30] C.Y. Shih, C.P. Wu, M.V. Shugaev, L.V. Zhigilei, Atomistic modeling of nanoparticle generation in short pulse laser ablation of thin metal films in water, Journal of Colloid and Interface Science, 489 (2017) 3-17.

[31] A. Nastulyavichus, S. Kudryashov, A. Ionin, Comparative Analysis of the Silver Nanoparticle's Yield for Pico-Femto-Nanosecond Laser Generation, Micromachines, 14 (2023).

[32] I. Rocha-Mendoza, S. Camacho-López, Y.Y. Luna-Palacios, Y. Esqueda-Barrón, M.A. Camacho-López, M. Camacho-López, G. Aguilar, Second-harmonic generation of ZnO nanoparticles synthesized by laser ablation of solids in liquids, Optics and Laser Technology, 99 (2018) 118-123.

[33] T. Smausz, G. Kecskeméti, B. Kondász, G. Papp, Z. Bengery, J. Kopniczky, B. Hopp, Nanoparticle Generation From Nitinol Target Using Pulsed Laser Ablation, Journal of Laser Micro Nanoengineering, 10 (2015) 171-174.

[34] I.N. Saraeva, S.I. Kudryashov, A.A. Rudenko, M.I. Zhilnikova, D.S. Ivanov, D.A. Zayarny, A.V. Simakin, A.A. Ionin, M.E. Garcia, Effect of fs/ps laser pulsewidth on ablation of metals and silicon in air and liquids, and on their nanoparticle yields, Applied Surface Science, 470 (2019) 1018-1034.

[35] S. Noël, J. Hermann, T. Itina, Investigation of nanoparticle generation during femtosecond laser ablation of metals, Applied Surface Science, 253 (2007) 6310-6315.

[36] N.C. Nayak, Y.C. Lam, C.Y. Yue, A.T. Sinha, CO₂-laser micromachining of PMMA:: the effect of polymer molecular weight, Journal of Micromechanics and Microengineering, 18 (2008).

[37] B.S. Shin, J.Y. Oh, H. Sohn, Theoretical and experimental investigations into laser ablation of polyimide and copper films with 355-nm Nd:YVO4 laser, Journal of Materials Processing Technology, 187-188 (2007) 260-263.

[38] L. Torrisi, S. Gammino, A.M. Mezzasalma, A.M. Visco, J. Badziak, P. Parys, J. Wolowski, E. Woryna, J. Krása, L. Láska, M. Pfeifer, K. Rohlena, F.P. Boody, Laser ablation of UHMWPE-polyethylene by 438 nm high energy pulsed laser, Applied Surface Science, 227 (2004) 164-174.

[39] L. Romoli, F. Fischer, R. Kling, A study on UV laser drilling of PEEK reinforced with carbon fibers, Optics and Lasers in Engineering, 50 (2012) 449-457.

[40] M. Womack, M. Vendan, P. Molian, Femtosecond pulsed laser ablation and deposition of thin films of polytetrafluoroethylene, Applied Surface Science, 221 (2004) 99-109.

[41] G.D. Kim, J.T. Rundel, B.K. Paul, UV laser ablation of polyetherimide embossing tools for the packaging of membranes and microchannels using sealing bosses, International Journal of Precision Engineering and Manufacturing, 11 (2010) 665-671.

[42] M.R. Kalus, N. Barsch, R. Streubel, E. Gokce, S. Barcikowski, B. Gokce, How persistent microbubbles shield nanoparticle productivity in laser synthesis of colloids - quantification of their volume, dwell dynamics, and gas composition, Phys Chem Chem Phys, 19 (2017) 7112-7123.

[43] M.R. Kalus, R. Lanyumba, N. Lorenzo-Parodi, M.A. Jochmann, K. Kerpen, U. Hagemann, T.C. Schmidt, S. Barcikowski, B. Gokce, Determining the role of redox-active materials during laser-induced water decomposition, Phys Chem Chem Phys, 21 (2019) 18636-18651.

[44] T. Fromme, L.K. Tintrop, S. Reichenberger, T.C. Schmidt, S. Barcikowski, Impact of Chemical and Physical Properties of Organic Solvents on the Gas and Hydrogen Formation during Laser Synthesis of Gold Nanoparticles, ChemPhysChem, 24 (2023) e202300089.

[45] L.M. Frias Batista, E. Kaplan, C. Weththasingha, B. Cook, S. Harris, A. Nag, K.M. Tibbetts, How Pulse Width Affects Laser Ablation of Organic Liquids, The Journal of Physical Chemistry B, 127 (2023) 6551-6561.

[46] I.I. Beilis, Laser plasma generation and plasma interaction with ablative target, Laser and Particle Beams, 25 (2007) 53-63.

[47] A.A. Ionin, S.I. Kudryashov, S.V. Makarov, A.A. Rudenko, P.N. Saltuganov, L.V. Seleznev, D.V. Sinitsyn, E.S. Sunchugasheva, Femtosecond laser fabrication of sub-diffraction nanoripples on wet Al surface in multi-filamentation regime: High optical harmonics effects?, Applied Surface Science, 292 (2014) 678-681.

[48] C. Wei, Y. Zhang, N. Sugita, Y. Ito, Generation mechanism and temporal–spatial evolution of electron excitation induced by an ultrashort pulse laser in zirconia ceramic, Applied Physics A, 130 (2024) 105.

[49] B. Stępak, M. Gazińska, M. Nejbauer, Y. Stepanenko, A. Antończak, Diverse nature of femtosecond laser ablation of poly(L-lactide) and the influence of filamentation on the polymer crystallization behaviour, Scientific Reports, 9 (2019) 3069.

[50] J. Fang, L. Zhang, D. Sutton, X. Wang, T. Lin, Needleless Melt-Electrospinning of Polypropylene Nanofibres, Journal of Nanomaterials, 2012 (2012) 382639.